



ELSEVIER

Available online at www.sciencedirect.com

SCIENCE @ DIRECT®

Combustion and Flame 141 (2005) 149–169

Combustion
and Flame

www.elsevier.com/locate/combustflame

Effects of sample orientation on nonpiloted ignition of thin poly(methyl methacrylate) sheet by a laser

1. Theoretical prediction

Yuji Nakamura ^{a,*}, Takashi Kashiwagi ^b

^a *EcoTopia Science Institute, Nagoya University, Furo-cho, Chikusa-ku, Nagoya 464-8603, Japan*

^b *The National Institute of Standards and Technology, Building Fire Research Laboratory, MS-8660 Gaithersburg, MD 20899-8665, USA*

Received 27 July 2004; received in revised form 1 December 2004; accepted 20 December 2004

Abstract

Nonpiloted ignition processes of a thin poly(methyl methacrylate) (PMMA) sheet (0.2 mm thick) with a laser beam as an external radiant source are investigated using three-dimensional, time-dependent numerical calculations. The effects of sample orientation angle on ignition delay time in quiescent air in a normal-gravity environment and of imposed velocity in a microgravity environment are determined. The numerical model includes heat and mass transport processes with global one-step chemical reactions in both gas and solid phases. A simple absorption model based on Beer's law is introduced and bulk absorption coefficients are applied to the solid PMMA and evolved methylmethacrylate (MMA). The PMMA sample surface is kept normal to the incident radiation at all sample orientation angles. In a zero gravity environment, ignition delay time increases with an increase in imposed flow velocity. In quiescent normal gravity, ignition delay time has a strong dependency on the sample orientation angle due to a complex interaction between the buoyancy-induced flow containing evolved MMA and the incident laser beam. Without absorption of the incident radiation by the evolved MMA, ignition is not achieved. The most favorable ignition configuration is the ceiling configuration (downward-facing horizontal sample irradiated by upward laser beam). The formation of a hole through the thin sample due to consumption has two counteractive effects on the ignition process: one is a reduction in the fuel supply rate, and the other is an increase in the air supply from the side opposite to the irradiated side by the buoyancy-induced flow through the hole. © 2005 The Combustion Institute. Published by Elsevier Inc. All rights reserved.

Keywords: Nonpiloted ignition; PMMA; Gravity; Hole formation; Prediction

1. Introduction

Ignition of a solid material is an important first step in any fire scenario. Ignition of solid materials has been examined by many researchers for decades, and we have found a book [1] as well as review articles [2,3] on this subject. There are two different ignition modes. One is piloted ignition and the other

* Corresponding author. Present address: Division of Mechanical Science, Hokkaido University, Kita 13 Nishi 8, Kita-ku, Sapporo 060-8628, Japan. Fax: +81-11-706-6386.

E-mail address: yuji-mg@eng.hokudai.ac.jp (Y. Nakamura).

Nomenclature

B	frequency factor [1/s, 1/min]	y	y direction [m]
c_p	specific heat of constant pressure [kJ/(kg K)]	z	z direction [m]
c_s	specific heat of PMMA . . . [kJ/(kg K)]	<i>Greek symbols</i>	
D	diffusivity [m ² /s]	α	ratio of the amount of MMA evolved from surfaces
E	activation energy [kJ/mol]	β	absorption coefficient Gas phase [1/(atm m)] Solid phase [1/m]
F	external force vector [N/m ³]	δ	thickness of solid [m]
h	enthalpy [kJ]	ε	surface emissivity
I	external radiation [kW/m ²]	ν	stoichiometric constant
k	thermal conductivity [kW/(m K)]	ρ	density [kg/m ³]
l	path length along the irradiative flux in gas phase [m]	σ	Stefan–Boltzman constant, 5.67 × 10 ⁻¹² [kW/(m ² K ⁴)]
M	molecular weight [kg/mol]	τ	stress tensor
\dot{m}	mass flux via decomposed reactions in solid [kg/(m ² s)]	$\dot{\omega}$	reaction rate Gas phase [kg/(m ³ s)] Solid phase [1/s]
n	normal to the surface [m]	<i>Sub-superscripts</i>	
p	pressure [Pa]	0	initial (ambient) state
Q	total radiant energy on the surface. [W]	ab	absorption
Q'	heat source term in the energy equation [kW/m ³]	ex	external radiation
q	heat of combustion of evolved products [kJ/kg]	G	gravity
r	surface reflectivity	g	gas phase
R	universal gas constant, 8.314 × 10 ⁻³ [kJ/(K mol)]	i	i th component
s	path length along the irradiative flux in the solid [m]	MMA	MMA vapor
T	temperature [K]	ox	oxygen
t	time [s]	p	pyrolysis reaction in the solid
u	velocity vector [m/s]	rad	irradiation center
U_{in}	imposed flow velocity in microgravity case [m/s]	react	reaction
u	velocity component in each direction [m/s]	surf	surface
X	mole fraction	S	solid phase
x	x direction [m]	x	x direction
Y	mass fraction	y	y direction
		z	z direction

is nonpiloted ignition. Three conditions are simultaneously required for achieving ignition of a solid material: sufficient amount of both *fuel* and *oxygen* to yield a flammable gaseous mixture, and a *high enough temperature* to initiate runaway oxidation reactions within this mixture. Once the solid temperature reaches its decomposition (i.e., pyrolysis) temperature when heated by an external ignition source, the gaseous degradation products are evolved from the surface and combustible gas components in the products mix with the ambient oxygen to form the combustible mixture over the surface. Piloted ignition (e.g., ignition by a hot wire or a small flame) requires only the first two conditions, whereas non-

piloted ignition (e.g., ignition by a laser) requires all three conditions. Nonpiloted ignition is often controlled by the heating process of the gas phase near the sample surface. If a solid is a charring material, the temperature of the char surface formed during the preignition period becomes high enough (due to low thermal conductivity of the char) to act as a “self-induced pilot,” yielding ignition near the surface. Such an ignition mode cannot be expected in general for a noncharring polymeric material whose overall degradation characteristic is endothermic; the surface temperature of the degrading solid does not remain high enough to initiate gas-phase oxidation reactions. Thus some other gas-phase heating process

is required to increase the temperature near the surface from that of the degrading surface high enough to initiate the runaway reactions. One possible heating process is high-temperature external flow over the material. Another possible heating process is absorption of external thermal radiation by a fuel gas being evolved from decomposition reactions of the material. To investigate the latter ignition process, a CO_2 laser is used as an external radiant source in this study due to ease of its power control, directional change, and on-and-off procedure.

The importance of radiant energy absorption by decomposed gaseous products from solid-phase reactions was addressed in mid-1970s. Kashiwagi [4] investigated the transmittance of a CO_2 laser used as an external radiant source through a plume of evolved degradation products when the laser beam irradiated the horizontally mounted polymer surface. A large reduction in transmittance was observed after the decomposition reaction started during the preignition period. The amount of reduction was found to differ between vertically and horizontally placed sample orientations (laser irradiation normal to the surface for both angles). These results demonstrate that the decomposed gaseous products absorb the incident radiation energy and play an important role in the observed transmittance decay. Another demonstration that involved igniting a liquid fuel pool with a CO_2 laser beam confirms the significant absorption of external radiant energy to raise gas-phase temperature from the boiling temperature of the liquid to a level high enough to cause ignition [5]. Following these observations, various research groups conducted numerical calculations to understand the detailed ignition processes, including the absorption of external radiant energy. Amos and Fernandez-Pello [6] performed numerical analysis with a simple absorption model in the stagnation point flow field. Park and T'ien [7] examined a two-dimensional ignition problem in the boundary layer flow system with a two-flux radiative transfer model. Di Blasi et al. [8] investigated two-dimensional, time-dependent solid combustion processes, including absorption in the gas phase and also in the solid phase, and addressed the relative importance of absorption effects in a zero-gravity environment. Thus, the importance of absorption of external radiant energy by the evolved degradation products has been well confirmed.

Much of the earlier work, however, was performed in a relatively simple flow field, not the three-dimensional flow field induced by a buoyancy force. Three-dimensional flow field effects induced by buoyancy are important for practical fire applications because the local gas temperature and species concentration distributions are strongly affected by the flow field induced by buoyancy. The

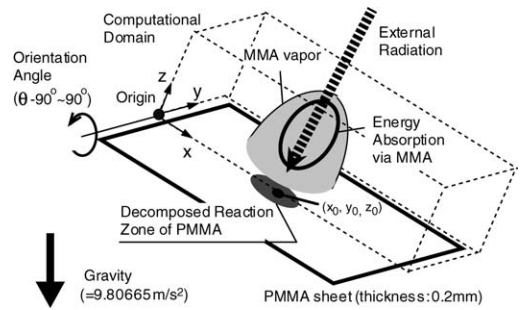


Fig. 1. Schematic of numerical model.

three-dimensional flow field induced by buoyancy is very complex, and it cannot be expressed as either a one-dimensional or two-dimensional boundary layer flow. Thus, the three-dimensional complex flow field induced by buoyancy force must be included to understand the role of absorption in ignition in normal gravity.

In the present study, imposed flow velocity (in a zero- g environment) and sample orientation angle in quiescent air (in a normal- g environment) are varied to investigate the interaction between absorption and transport processes. The objective of this study is to understand the ignition processes of a thin poly(methyl methacrylate) (PMMA) sheet with a laser beam as an external radiant source.

2. Model description

Fig. 1 is a schematic illustration of the physical configuration. A thin PMMA sample 0.2 mm thick is placed in air and a radiant flux is imposed normal to the surface. Once the sample heats up to its pyrolysis temperature (650–700 K), decomposed gas (MMA) evolves from the surface. MMA vapor has an absorption band at the incident radiation wavelength and is considered the energy-absorbing medium. Evolved MMA mixes with ambient oxygen to form the combustible mixture over the irradiated surface. Because the laser beam passes through the mixture, the mixture absorbs the incident energy and this increases the local temperature, leading to ignition. Since PMMA is a noncharring material, the surface temperature remains around the decomposition temperature (650–700 K). At this surface temperature, heat transfer from the hot surface to the gas phase is not sufficient to lead the gas-phase ignition. No ignition is achieved when the vapor phase absorption contribution is excluded from the calculation, indicating that absorption by MMA must play a key role in ignition.

In a zero- g environment the imposed flow velocity, U_{in} , which is parallel to the PMMA surface, is varied from 0.02 to 0.4 m/s to determine the effects of the interaction between a MMA plume and the laser

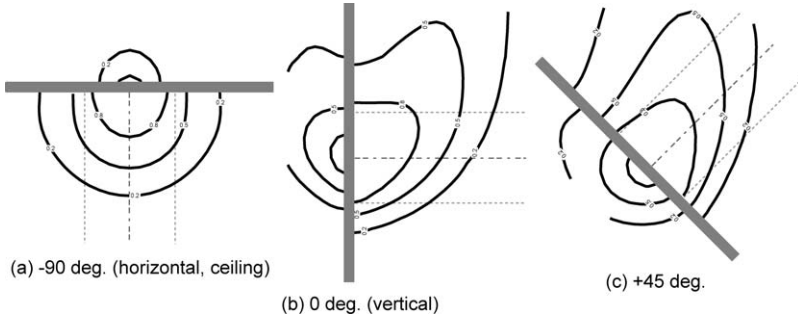


Fig. 2. Schematics of typical MMA plume shape in normal-g condition.

beam on ignition delay time. In a normal quiescent gravity environment, the sample is rotated from $\theta = -90^\circ$ (horizontally placed sample irradiated from beneath, a ceiling configuration) to $\theta = 90^\circ$ (horizontally placed and irradiated from above, a floor configuration). Fig. 2 shows the schematics of the MMA plume prior to the ignition event at various sample angles. The change in sample orientation angle (note that incident radiation poses always normal to the surface) modifies the interaction between the MMA plume and the incident laser beam due to buoyancy-induced flow. The laser beam, whose total power is in the range of 17–27 W, is continuously applied at a constant level until ignition occurs. Continuous irradiation eventually causes complete consumption of the PMMA and makes a hole through the sample; this study investigates the effects of the formation of the hole on ignition processes. The irradiation profile is a Gaussian distribution (a half-width at a half-value of the peak flux is about 2.0 mm) and its center is on the z axis. The time $t = 0$ s is defined when the sample is first exposed to irradiation. Physical coordinates are drawn as seen in Fig. 1 and the computational domain is $48 \times 20 \times 62.1$ mm in the x , y , z direction, respectively. The sample is placed on the x – y plane. Since the flow field is symmetric at the $y = 0$ surface, only one side of the y direction is calculated.

2.1. Gas-phase model

Time-dependent conservation equations of mass, energy, momentum (Navier–Stokes equation), and species concentration are numerically solved; they are described below. Note that the chemical reaction in the gas phase, i.e., oxidative reaction of MMA, is modeled as a global one-step, irreversible reaction.

Mass

$$\frac{\partial \rho_g}{\partial t} + \nabla \cdot (\rho_g \mathbf{u}) = 0. \quad (1)$$

Momentum

$$\rho_g \left(\frac{\partial \mathbf{u}}{\partial t} + (\mathbf{u} \cdot \nabla) \mathbf{u} \right) + \nabla p = \mathbf{F}_G + \nabla \cdot \boldsymbol{\tau}. \quad (2)$$

Energy

$$\begin{aligned} \frac{\partial}{\partial t} (\rho_g h_g) + \nabla \cdot (\rho_g \mathbf{u} h_g) \\ = q_g \dot{\omega}_g + Q'_{g,ab} + \nabla \cdot k_g \nabla T_g \\ + \nabla \cdot \sum_i h_{g,i} (\rho_g D)_i \nabla Y_{g,i}. \end{aligned} \quad (3)$$

Species

$$\begin{aligned} \frac{\partial}{\partial t} (\rho_g Y_{g,i}) + \nabla \cdot (\rho_g \mathbf{u} Y_{g,i}) \\ = \nabla \cdot (\rho_g D)_i \nabla Y_{g,i} - \nu_{g,i} \dot{\omega}_g. \end{aligned} \quad (4)$$

Equation of state

$$p_0 = \rho_g T_g R \sum \left(\frac{Y_{g,i}}{M_i} \right) = \rho_g T_g R / M. \quad (5)$$

Reaction rate

$$\begin{aligned} \dot{\omega}_g = B_g \rho_g Y_{g,MMA} Y_{g,ox} \exp \left(-\frac{E_g}{RT_g} \right), \\ i = ox, MMA. \end{aligned} \quad (6)$$

These equations are almost the same as those used in our previous publication [9] except for the additional energy absorption term in the gas phase. The corresponding energy absorption term is given according to the Beer's law and is expressed as

$$Q'_{g,ab} = -dI(\ell)/d\ell = I(\ell) p_0 \beta X_{g,MMA}(\ell), \quad (7)$$

where I [kW/m^2] is the incident radiation, β [$\text{atm}^{-1} \text{m}^{-1}$] is the absorption coefficient of MMA vapor, p_0 [atm] is the ambient pressure ($= 1$), $X_{g,MMA}$ is the mole fraction of MMA and ℓ is the distance from the tip of the plume in the z direction. Note that MMA is assumed to act only as an absorber of the incident radiation, not as an emitter. Therefore, it is assumed that no gaseous components lose their energy by thermal re-emission. Moreover, because the radiant energy emitted from the hot surface is quite small compared with the incident radiation, absorption of the emission from the hot surface by MMA is neglected.

Table 1
Physical and chemical constants

Gas phase [6,10,11]			
β	absorption coefficient [$\text{atm}^{-1} \text{m}^{-1}$]	10	[6]
A_g	frequency factor of reaction [$\text{m}^3/(\text{mol s})$]	1.4×10^9	[10]
E_g	activation energy of reaction [kJ/mol]	142	[10]
q_g	heat of combustion [kJ/kg]	26,000	[11]
$v_{g,\text{MMA}}$	stoichiometric constant for MMA	1.0	
$v_{g,\text{ox}}$	stoichiometric constant for oxygen	1.92	
Solid phase [11–14]			
c_S	specific heat [$\text{kJ}/(\text{kg K})$]	$1.84 + 2.38 \times 10^{-3} (T - T_0)$	[12]
k_S	heat conductivity [$\text{J}/(\text{K m s})$]	$0.193 + 2.5 \times 10^{-4} (T - T_0)$	[12]
A_S	frequency factor of reaction [$1/\text{s}$]	2.1×10^{15}	[13]
E_S	activation energy of reaction [kJ/mol]	210	[13]
q_S	heat of decomposition [kJ/kg]	1358	[11]
r	surface reflectivity	0.31	[14]
β_S	absorption coefficient of PMMA [m^{-1}]	150^a	
δ	sample thickness [m]	2.0×10^{-4}	
ε	emissivity of the surface	0.9	[14]
ρ_S	initial PMMA density [kg/m^3]	1190	[11]

^a The value was determined by fitting Beer's law for the measured transmittance through a 200- μm -thick PMMA sheet using a Mattson Instruments Galaxy 7020 FTIR with a resolution of 1 cm^{-1} at the laser lines.

Boundary conditions are imposed as zero gradients of temperature, species concentrations, and dynamic pressure to simulate the open boundaries, except at the $y = 0$ plane (symmetric) and the PMMA surface (interfacial). At the PMMA surface, the dependent variables are solved with interfacial boundary conditions [9]. Specific heat at constant pressure is given by a linear function of the local temperature. The physical and chemical properties used in the calculation are listed in Table 1.

2.2. Solid-phase model

In the solid phase, time-dependent mass and energy conservation equations are solved. Note that the chemical reaction in the solid-phase is modeled as a global one-step, irreversible pyrolysis reaction and the degradation product (MMA) of PMMA evolves *immediately* after the degradation, which reduces the local density of PMMA (same volume but less mass). As PMMA is a noncharring material, no residue remains after the pyrolysis reaction; i.e., the species in the solid phase is PMMA only. The corresponding conservation equations are as follows.

Mass

$$\frac{\partial(\rho_S/\rho_{S0})}{\partial t} = -\dot{\omega}_p. \quad (8)$$

Energy

$$\rho_S c_S \frac{\partial T_S}{\partial t} = (q_p \dot{\omega}_p) \rho_{S0} + \nabla \cdot (k_S \nabla T_S) + Q'_{S,\text{ab}}. \quad (9)$$

Reaction rate

$$\dot{\omega}_p = B_p \left(\frac{\rho_S}{\rho_{S0}} \right) \exp \left(-\frac{E_p}{RT_S} \right). \quad (10)$$

In the present model, we exclude our previously used “thermally thin” approximation [9], although the sample thickness is relatively thin ($\sim 0.2 \text{ mm}$). However, this approximation is not valid when a high heating rate is applied as is the case in this study. Three-dimensional heat transfer in the solid is computed because the temperature gradient along the x and y axes may be steep due to the Gaussian distribution of the incident radiation. In-depth absorption is taken into account; the incident radiation decays according to the Beer's law as expressed by

$$Q'_{S,\text{ab}} = -dI(s)/ds = I(s) \cdot \beta_S \cdot \rho_S(s)/\rho_{S0}(s), \quad (11)$$

where I [kW/m^2] is incident radiation at the exposed surface, β_S [m^{-1}] is absorption coefficient of PMMA, ρ_S is the local density of the solid, and s is the distance from the exposed surface. As described in the energy equation, the pyrolysis reaction occurs not only at the surface but also inside the solid. The oxidative reaction of PMMA is excluded as it is negligible due to slow diffusion of oxygen to the surface compared with the rapid heating rates used in this work. At the surface, dependent variables are solved with the interfacial boundary conditions described below.

2.3. Interfacial boundary conditions

The following are applied as interfacial boundary conditions:

$$u_x = u_y = 0.0,$$

$$u_z = \dot{m} / \rho_g,$$

$$k_g \frac{\partial T_g}{\partial n} = k_S \frac{\partial T_S}{\partial n} + \varepsilon \sigma (T_{\text{surf}}^4 - T_0^4) + \dot{m} h_g |_{\text{surf}},$$

$$\dot{m} Y_{g,i} - (\rho_g D \nabla Y_{g,i} |_{\text{surf}}) = \dot{m}_i,$$

where

$$\dot{m}_{\text{ox}} = 0.0 \quad \text{and} \quad \dot{m}_{\text{MMA}} = \alpha \int \dot{\omega}_p d\delta.$$

α is ratio of the amount of MMA evolved from the irradiated/backside surfaces and its details are given in the next section. Surface reradiation is taken into account with the assumption of a gray body. Convective heat loss from the hot surface is taken into account (the last term in the T_{surf} boundary condition) because it may not be negligible at some of the sample angle orientations. Physical and chemical constants are listed in Table 1, as are those of the gas phase.

2.4. Model of evolved product through the solid

In the present study, the degradation reaction of the solid can occur through its volume, right up to the surface. The transport process of MMA produced inside the solid is assumed to be infinitely fast in the z direction only (no MMA transport in x and y axes) and it is evolved immediately into the atmosphere from either the irradiated surface or the back surface. Since the transport process of MMA is not actually solved, it is difficult to determine the ratio of the amount of MMA evolved from the two surfaces although the total amount is known. Thus, one additional model to describe the MMA mass flux from each surface must be introduced.

In this study, it is assumed that the transport direction of the product gas is determined by the distribution of solid density; *MMA moves always toward the lower density*. For example, consider the computational cell inside the solid A whose density is ρ_A . The cell is between two neighbor cells B and C (in-depth direction) whose densities are ρ_B (for above-neighbored cell) and ρ_C (for below-neighbored cell) (see details in Fig. 3). Suppose ρ_A is greater than ρ_B and ρ_A is smaller than ρ_C , the decomposed gas produced at the center cell (of A) is evolved from the irradiated surface. For the cell located at the boundary to the gas phase, the same reasoning can be applied due to the fact that the density of the gas phase is much smaller than that of the solid phase. The gas from the “boundary” cell must be evolved from the “boundary” surface. There may occur a case in which ρ_A is greater than ρ_B and ρ_A is also greater than ρ_C . In this case the gas produced at the center cell A evolves from both surfaces in equal amounts. In the case where ρ_A is smaller than ρ_B and ρ_A is

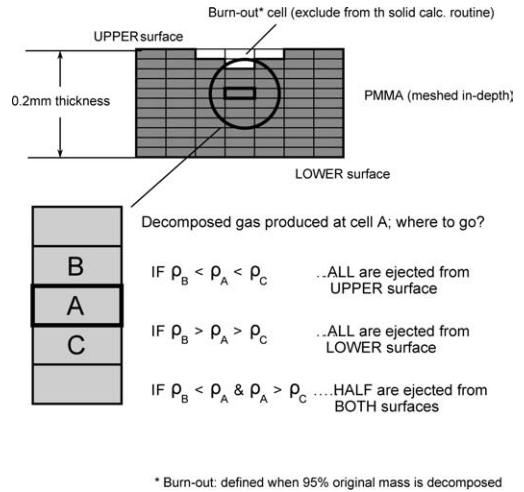


Fig. 3. Schematics of solid decomposition model.

also smaller than ρ_C , which may rarely occur, the gas production from cell A is neglected. Once the local density is less than 5% of its original (i.e., 95% PMMA is decomposed), the computational cell in the solid is considered to be consumed and excluded from the calculation routine. In this manner, each computational solid cell is consumed in turn until the entire local PMMA is consumed in the in-depth direction; i.e., a hole is opened (see Fig. 4). However, all ignition phenomena observed in this study are those before the hole is made.

3. Numerical method

All calculations are made with a modified version of Fire Dynamic Simulator (FDS) developed by the National Institute of Standards and Technology (NIST) [15]. Additional subroutines are developed to solve the solid phase and the energy absorption by MMA vapor as well as PMMA coupled with the original FDS. FDS is based on the finite volume method, and it has second-order accuracy in time and space. FDS has two modes to run: direct numerical simulation (DNS) and large eddy simulation (LES). All simulation results presented here are conducted in the DNS mode. The total number of grid points is 138,000 ($50 \times 40 \times 69$) and a nonuniform grid system is applied in the x and z directions. The minimum-size grid (0.35 mm) is placed near the surface and the irradiated center to accurately resolve the local ignition location. Since gas quantities and solid quantities are coupled to each other only through the interfacial condition, the calculation routine is completely separated in each phase. Therefore, we take a PMMA sample corresponding to one-cell thickness in the gas-phase grid, while it is divided into 20 nodes in the

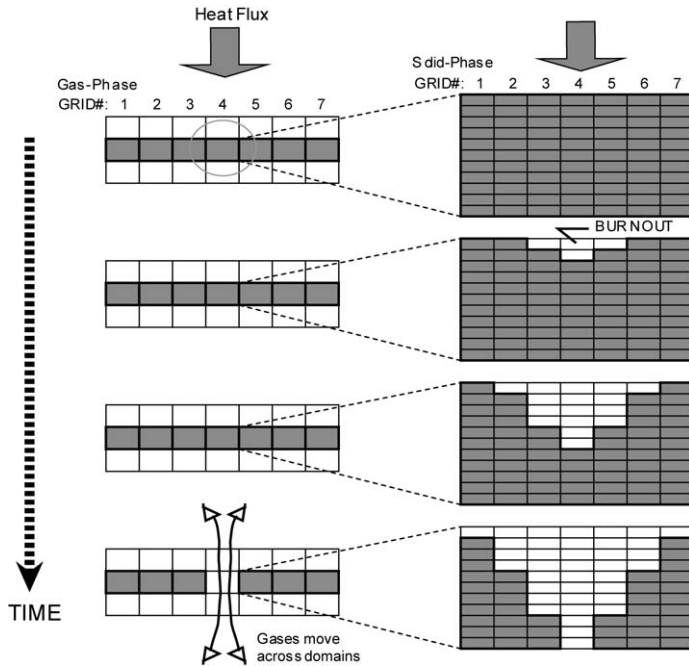


Fig. 4. Schematics of gas–solid-phase grid system and concept of “opened” cell.

in-depth direction in the solid-phase calculation to solve solid-phase quantities accurately (i.e., the gas-phase grid cell is 20 times larger than the solid-phase grid cell). Although solid decomposition is taken into account in the current model, the solid-phase grid is converted to the gas-phase grid only when an entire in-depth solid is consumed, as seen in Fig. 4. A typical CPU time for one productive run is about 72 h on a generic personal computer (Pentium-III level).

4. Results and discussion

4.1. Ignition criterion

Ignition is always achieved at the $y = 0$ plane (due to symmetry). Since the ignition is a localized as well as a rapid phenomenon, two important properties are introduced to discuss the ignition behavior. One is ignition delay time, t_{ig} ; the other is ignition location (x_{ig} , z_{ig}). The ignition criterion in the present study is defined as an instantaneous, local heat release rate that exceeds 3.0×10^4 kW/m³ [16].

4.2. Ignition delay time (t_{ig}) in zero-g and normal-g

Fig. 5 shows the effects of an imposed flow velocity (a: zero-g) and sample orientation angle (b: normal-g) on ignition delay time. Ignition delay time increases monotonically with an increase in imposed flow velocity in zero-g. In normal-g, on the

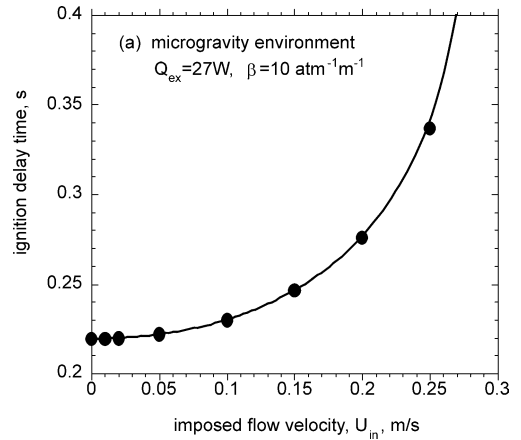


Fig. 5. Effects of (a) imposed flow velocity (in zero-g) and (b) sample orientation angle (in quiescent normal-g) on ignition delay time. Dashed line in (b) shows the hole opening time.

other hand, ignition delay time has a complex dependency on the orientation angle, and this trend is consistent for various imposed radiant powers as well as values of the absorption coefficient of MMA used in this study. It can be classified into approximately three regimes depending on the orientation angle. In regime 1, the ignition delay time increases with an increase in sample orientation angle from $\theta = -90^\circ$ until one gets to regime 2, where ignition delay time decreases with an increase in angle or becomes in-

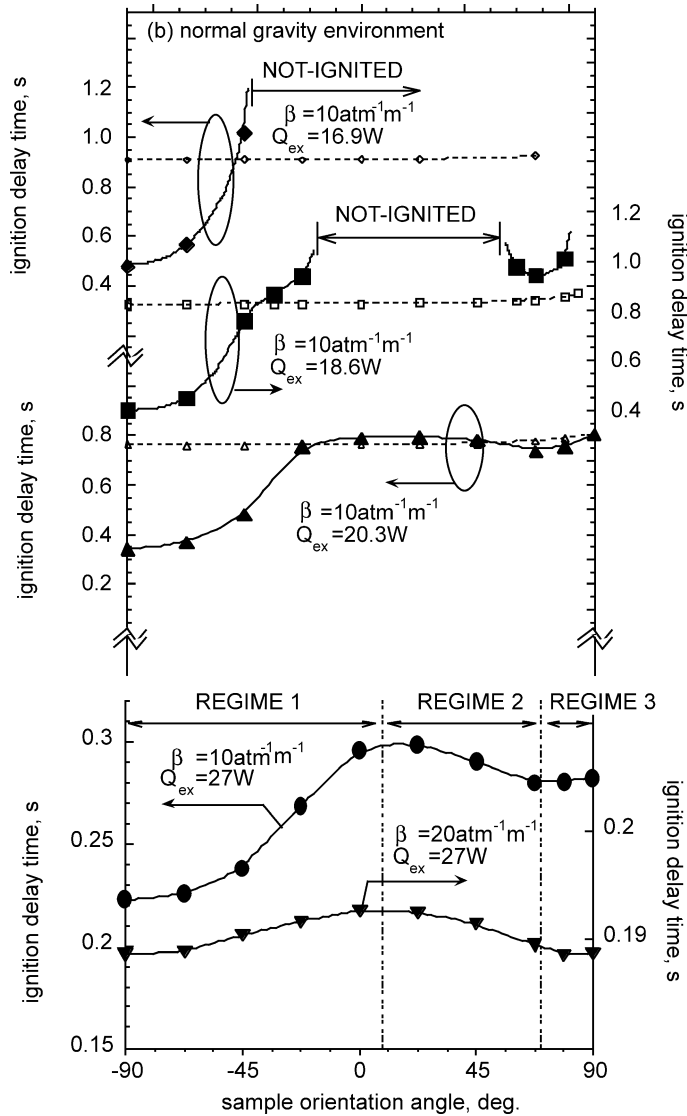


Fig. 5. Continued.

dependent of angle, or no ignition is achieved at low incident radiant energies. Finally the trend in regime 3 depends on values of incident radiant energy and absorption coefficient but encompasses angles from about +60° to +90°. Ignition delay time in regime 3 tends to be shorter than in regime 2 and onset of ignition is predicted at a total radiant energy of 18.6 W, at which no ignition is predicted in the regime 2. In Fig. 5b, the time when a small hole through the sample is also plotted at three incident total radiant energies of 20.3, 18.6, and 16.9 W. For 27 W, ignition always occurs before the hole opening. In regime 1, most ignitions occur before the appearance of a hole. However, ignition occurs after the appearance

of a hole in regime 2, except at an incident total radiant energy of 27 W. At an incident total radiant energy of 18.6 W, ignition occurs after the appearance of a hole in regime 3. Although the effects of a hole on ignition behavior appear to be negligible at 20.3 W because ignition occurs shortly after the appearance of the hole (it is a very small hole initially due to the Gaussian profile of the incident radiant energy distribution), the hole might have significant effects on cases in regime 3 (such as at an angle of +68°) at 18.6 W. The effects of the hole on ignition are discussed in more detail later. The results illustrated in Fig. 5b also indicate significant effects of the value of the absorption coefficient on ignition delay time. At 27 W, ignition time is greatly reduced

by doubling the MMA absorption coefficient, in particular, in regimes 2 and 3. This also indicates that nonpiloted ignition delay time consists not only of sample heatup time but also of gas-phase heating time.

The distinct difference in ignition delay time trends between zero- g and normal- g implies that buoyancy-induced flow plays a key role in the ignition event. However, at high incident flux or with a high absorption coefficient, ignition occurs shortly after the release of MMA to the gas phase, and interaction of the MMA plume with the incident laser beam does not significantly change with orientation angle; the effects of angle on ignition delay time decreases, as is shown in the case at 27 W with $\beta = 20 \text{ atm}^{-1} \text{ m}^{-1}$. Although five different cases are shown in Fig. 5b, two cases (case I, in which ignition occurs in all angles, and case II, in which ignition does not occur for a certain range of angles) are selected to analyze the ignition process in more detail.

4.2.1. Case I (at $Q_{\text{ex}} = 27 \text{ W}$ with $\beta = 10 \text{ atm}^{-1} \text{ m}^{-1}$)

Figs. 6–8 show the time-dependent ignition process induced by the absorption of incident radiant energy by the evolved degradation product of MMA. They show the formation of the MMA vapor plume, increase in local temperature, and finally onset of ignition. Figs. 6–8 illustrate cases (1) $\theta = -90^\circ$ (horizontally oriented and irradiated upward from the bottom, ceiling condition), (2) $\theta = 0^\circ$ (vertically oriented), and (3) $\theta = +45^\circ$ (upward-facing sample irradiated by the downward-directed beam), respectively.

The simulated results show that ignition always occurs in the gas phase away from the irradiated surface, within the region along the laser beam, irrespective of the sample orientation angle. Ignition delay time and ignition location vary depending on the sample orientation angle, suggesting that the strong interaction between the evolved MMA and the incident radiation beam plays a key role in the ignition process. Although laser energy absorption is the key cause of ignition, ignition occurs at a location where the radiant flux in the laser beam is not at its maximum (i.e., not along the center axis of the beam). Because the flow field as well as the MMA concentration profile is strongly affected by buoyancy, the ignition process is complex at various sample orientation angles. It is noted that the interaction length of the laser beam path with the MMA plume is the shortest at $\theta = -90^\circ$, followed by the case at $\theta = 0^\circ$, and longer in the case at $\theta = +45^\circ$. This difference affects the amount of absorption and subsequently the ignition process.

Figs. 9 and 10 illustrate the effects of sample orientation angle on ignition location (x_{ig} , z_{ig}). Fig. 9

shows the ignition locations and instantaneous MMA concentration contour plots at various sample orientation angles. Note that the solid circle denotes the ignition location at the angle denoted on a given figure and open circles represent all ignition locations corresponding to various other angles. These circles are used to show the relationship between the ignition location and the sample orientation angle. Fig. 10 shows the ignition locations expressed in x and z coordinates as a function of the orientation angle.

It appears that the qualitative relationship between the ignition location on the x axis and the sample orientation angle, as shown in Fig. 10, is somewhat similar to that between the ignition delay time and the sample orientation angle (Fig. 5b). In regime 1, where ignition delay time always increases with an increase in orientation angle, the ignition location moves away from the sample surface as well as from the center axis. In regimes 2 and 3, where ignition delay time decreases with the increase in orientation angle, the ignition location still moves away from the surface but it moves closer to the center axis (higher incident flux) with an increase in angle (the reduction in the x coordinate is much steeper than the increase in the z coordinate). These trends illustrate how ignition delay time is coupled with ignition location.

Fig. 11 shows the transmission of the incident heat flux through MMA plumes along the irradiated center axis at various orientation angles (vertical configuration = 0° , $+45^\circ$, $+68^\circ$, $+79^\circ$, floor configuration = $+90^\circ$) prior to ignition ($t = 0.28 \text{ s}$). Radiative flux shown in the figure is normalized by the incident peak flux. In the figure, it is seen that absorption of the incident heat flux starts from a significant distance (about 2 cm) from the sample surface because the large positive angles make taller MMA plumes. The amount of absorption exhibits a nonlinear relationship with the orientation angle: a small difference is observed between the vertical case and the $+45^\circ$ case, while a significant difference is observed between $+68^\circ$ and $+90^\circ$ (floor configuration). The amount of absorption is at most 10% of the original energy evolved by the MMA plume before ignition.

Ignition delay time can be classified into two parts: one (in an early stage) is the solid heatup time and the other (in a later stage) is the gas heatup time. The former is the time until the solid temperature reaches its pyrolysis temperature and no significant amount of decomposed gas is evolved until the end of this period (“solid-phase heating period”). A majority of the ignition delay time is solid heating time in the *piloted* ignition mode, whereas the latter is the time during which the evolved MMA mixes with surrounding air and the mixture achieves runaway gas-phase reactions (ignition) after the mixture temperature increases

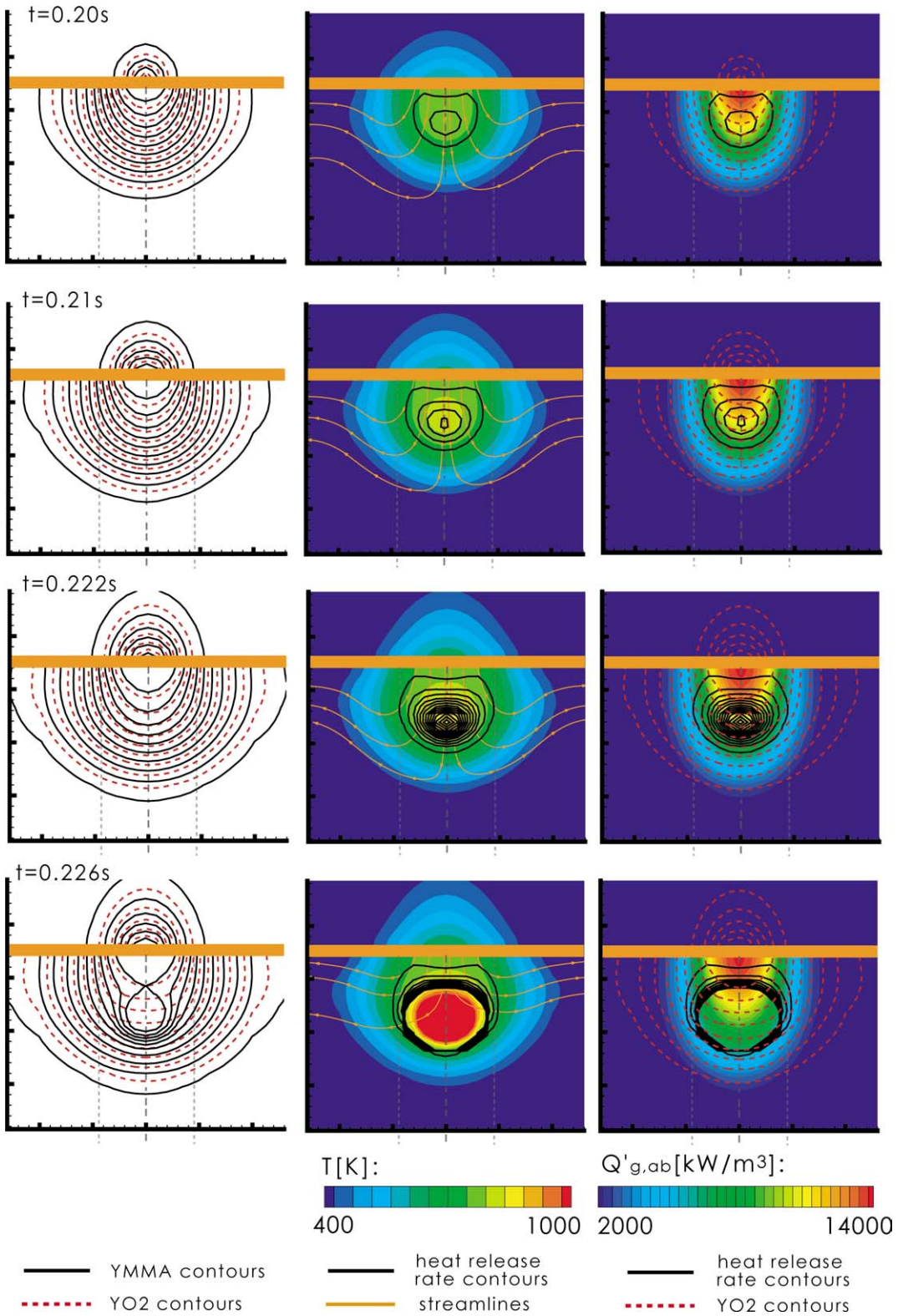


Fig. 6. Time sequence of two-dimensional dependent variable distributions on ceiling configuration ($\theta = -90^\circ$).

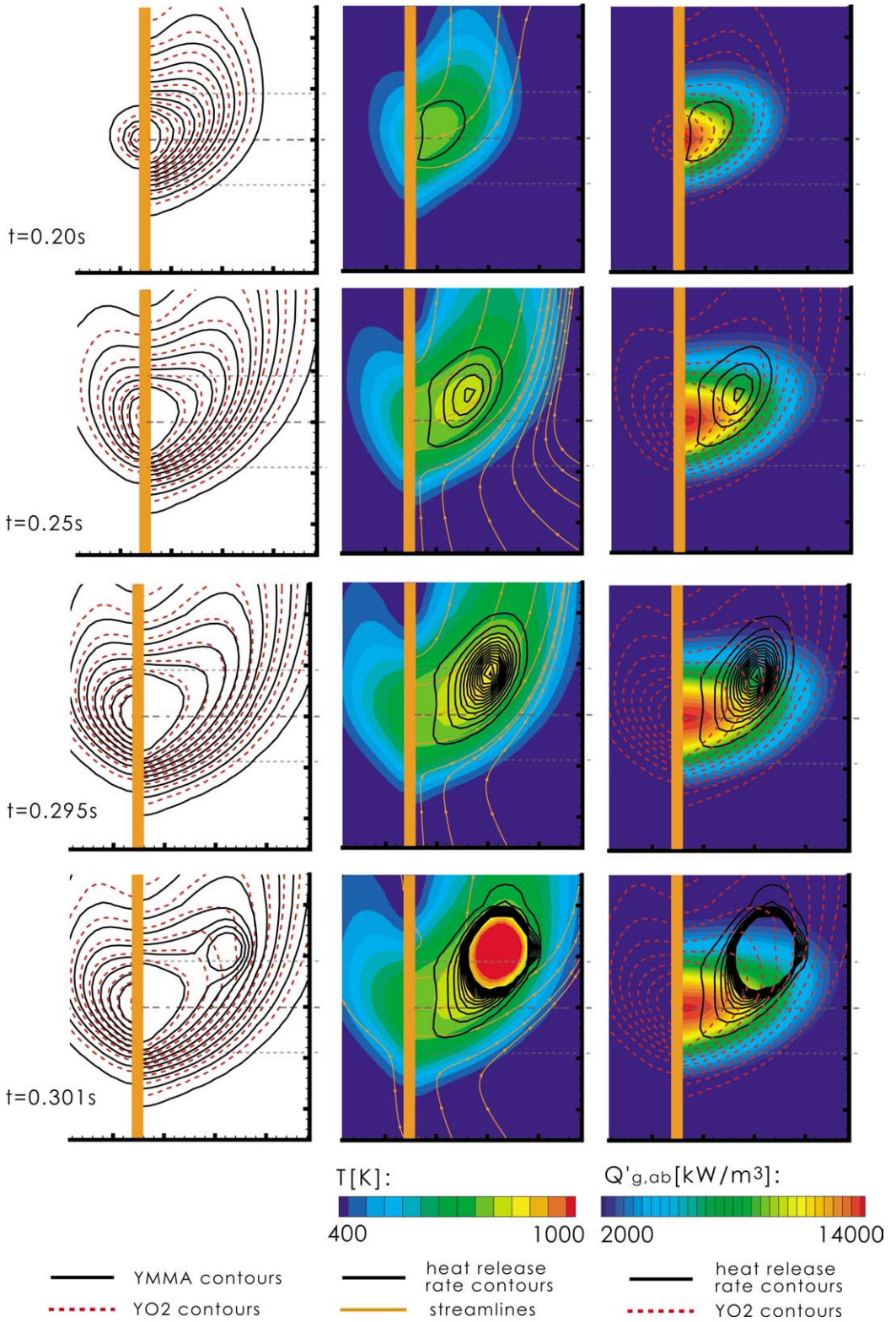


Fig. 7. Time sequence of two-dimensional dependent variable distributions on vertical configuration ($\theta = 0^\circ$).

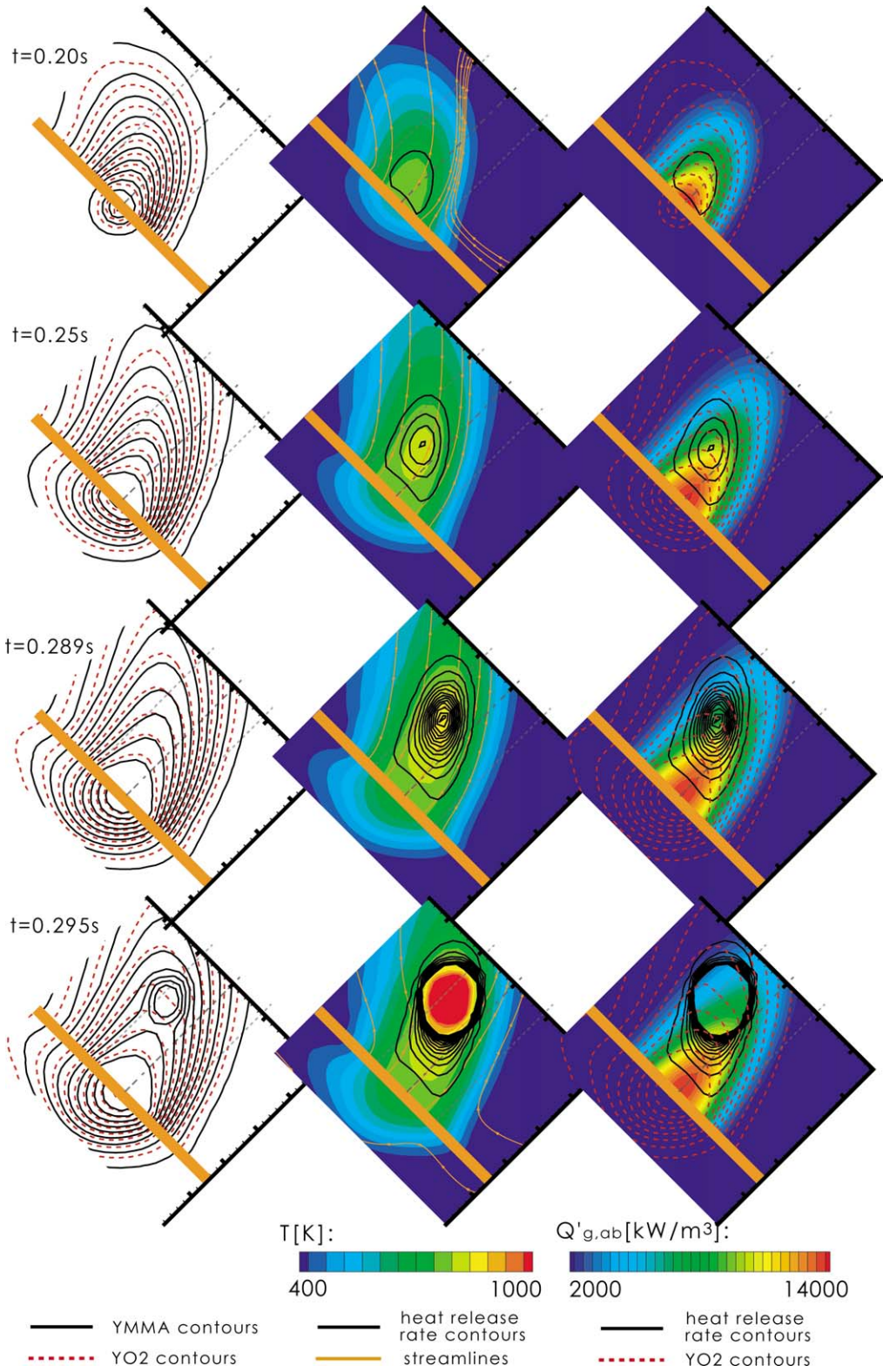


Fig. 8. Time sequence of two-dimensional dependent variable distributions on positively angled configuration ($\theta = +45^\circ$).

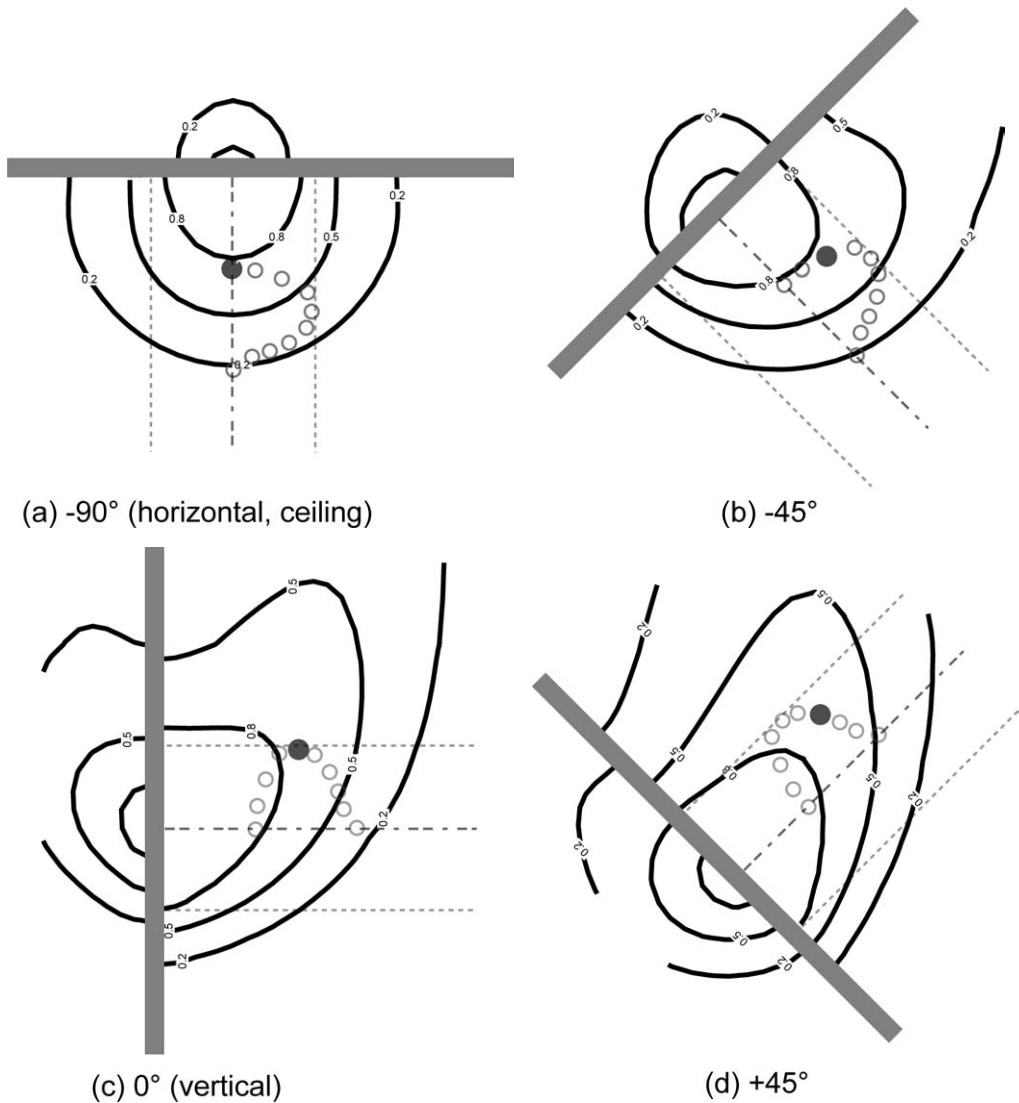


Fig. 9. Schematically illustration of ignition location in various angles. Imposed condition is $Q_{ex} = 27 \text{ W}$, $\beta = 10 \text{ atm}^{-1} \text{ m}^{-1}$.

enough by absorption/reaction/transport processes (“gas-phase heating period”). During the “gas-phase heating period,” another important time duration, the “evolution time,” can be defined as the time it takes the evolved degradation gas to travel from the surface to the ignition location. Fig. 12a shows ignition delay time and the three individual durations as a function of sample orientation angle. The results demonstrate that the solid heating time is nearly constant irrespective of the angle. The evolution time is very short compared with the total gas-phase heating time (they are roughly 6–9% depending on the angle). Fig. 12b shows the normalized version of Fig. 12a (normalized by the total ignition delay time at the given angle). The results demonstrate that the solid-phase heat-

ing time is nearly 60% of total ignition delay time, and this percentage is higher in the ceiling configuration (-90° case). It becomes a minimum at slightly past the vertical configuration ($\sim 0^\circ$ case). Thus, the gas-phase heating time is about the same as the solid-phase heating time in this configuration. This implies that a longer interaction time between the laser beam and a MMA plume is required for a nearly vertical sample to meet the ignition condition.

As discussed above, evolved MMA not only mixes with the ambient oxygen to form the combustible mixture, but also acts as an energy absorber in the gas phase. As the mixture is formed immediately after the MMA vapor is evolved (as seen in Figs. 6–8 at $t = 0.20 \text{ s}$), the heating up process of the mixture

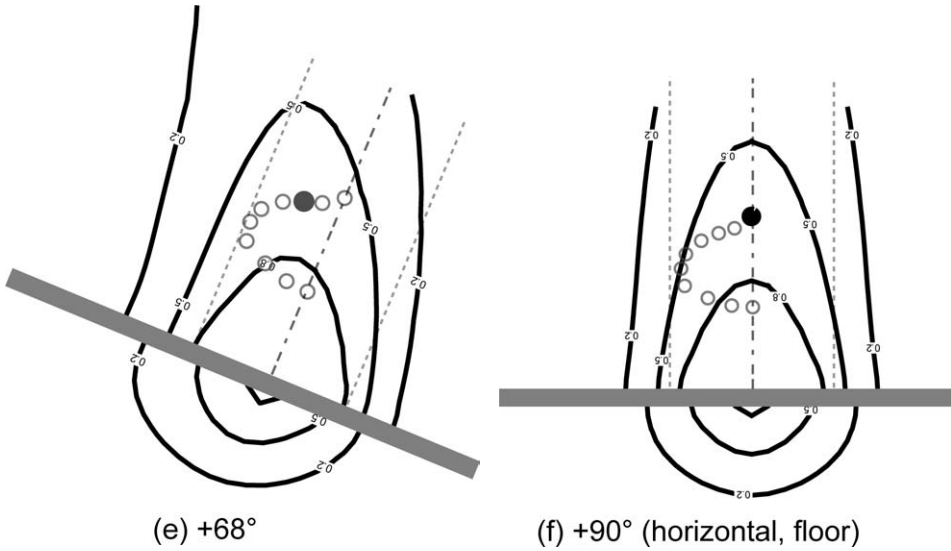


Fig. 9. Continued.

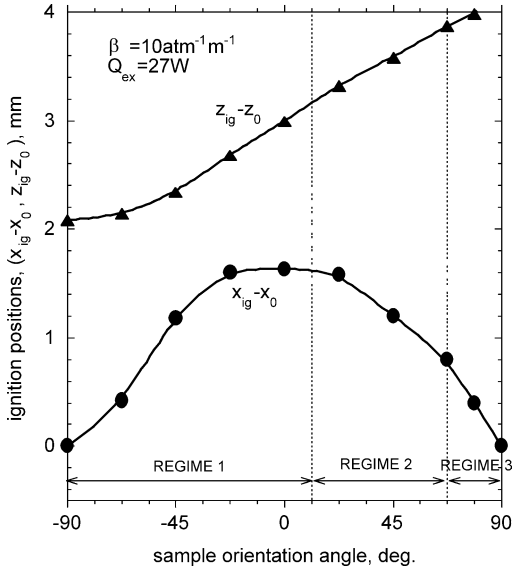


Fig. 10. Effects of sample orientation angle on ignition location (x_{ig} , z_{ig}). Imposed condition is $Q_{ex} = 27 \text{ W}$, $\beta = 10 \text{ atm}^{-1} \text{ m}^{-1}$.

must be key to determining whether ignition occurs or not. The observed complex ignition behavior could be explained by investigating how the local gas temperature increases enough to initiate a thermal runaway condition. Fig. 13 shows time histories of each energy source term of convection, diffusion, reaction, and absorption along the trajectories of the fuel gas pocket from the sample surface (which eventually ignites) during the evolution time at various sample orientation angles. A positive sign means that the term contributes to an increase in local temperature,

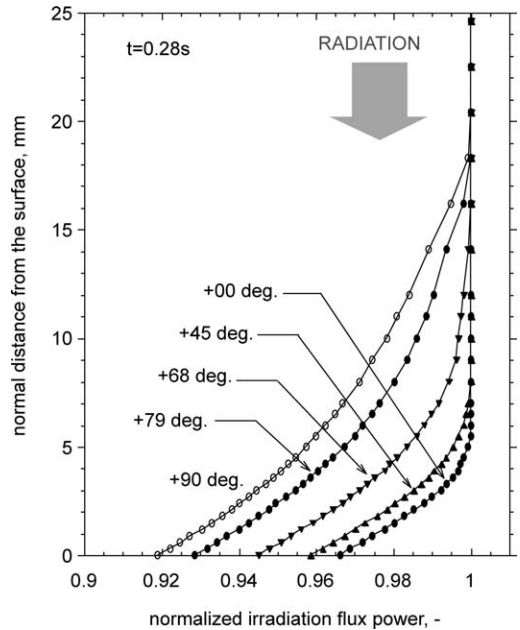


Fig. 11. Transmission of incident flux at various sample orientation angles with $Q_{ex} = 27 \text{ W}$ and $\beta = 10 \text{ atm}^{-1} \text{ m}^{-1}$ at $t = 0.28 \text{ s}$.

while a negative sign means cooling local temperature (therefore the sum of the four terms indicates the time derivative of local enthalpy). Time zero indicates the instant when the ignited gas is evolved from the surface. The results show that absorption makes the largest contribution, followed by convection initially. Once the temperature of the mixture is high enough, exothermic chemical reaction is accelerated and becomes the dominant contributor to further increases in

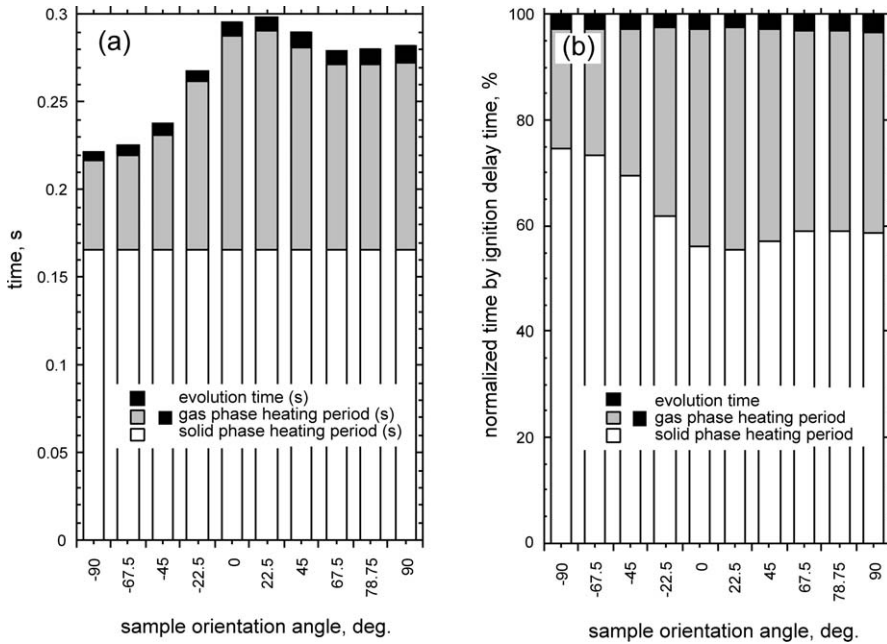


Fig. 12. Gas–solid-phase heating times in ignition delay times with respect to the sample angles at $Q_{ex} = 27 \text{ W}$, $\beta = 10 \text{ atm}^{-1} \text{ m}^{-1}$: (a) actual times, (b) nondimensional times (normalized by each ignition delay time).

the temperature to reach runaway reaction (ignition). This trend is the same for all orientation angles. As described earlier, ignition is defined when the local heat release rate ($q_g \dot{\omega}_g$) reaches $3 \times 10^4 \text{ kW/m}^3$. Since the energy supply rate by absorption is in the range of 1×10^4 to $1.5 \times 10^4 \text{ kW/m}^3$ irrespective of orientation angle, it corresponds to 30–50% of the energy needed to attain ignition. Convective heating of local temperature is positive initially but becomes near zero near the onset of ignition.

4.2.2. Case II ($Q_{ex} = 18.6 \text{ W}$ with $\beta = 10 \text{ atm}^{-1} \text{ m}^{-1}$)

For this condition, ignition delay time increases with an increase in the sample orientation angle from $\theta = -90^\circ$ to about $\theta = -30^\circ$ and ignition is not achieved in the angle range of approximately $-30 < \theta < +45^\circ$. However, ignition occurs in the angle range of approximately $+45^\circ < \theta < +80^\circ$. The first appearance of a hole through the sample is at about 0.85 s and is nearly independent of the sample angle, as shown in Fig. 5b. It is important to understand why ignition is not achieved in the second regime of the orientation angle. In this regime, ignition is achieved after formation of the hole through the sample if ignition occurs at all. Fig. 14a shows the distributions of absorbed energy contour and MMA mass fraction contour with temperature isotherms at $\theta = 0^\circ$ (vertical sample). At $t = 0.84 \text{ s}$, a hole appears and relatively strong absorption of the incident energy occurs

close to the irradiated sample surface, but the heat release rate (proportional to gas phase reaction rate) is not large enough to achieve a runaway condition, as shown in Fig. 14b. With an increase in time, the hole grows larger due to further consumption of the sample, and flow through the hole increases. The flow supplies warm air from the backside to the hot irradiated side. This increases heat release rate (as shown in Fig. 14b), but the amount of absorbed incident energy tends to gradually decrease as shown in Fig. 14a. It appears that consumption of the thin sample (decline in fuel supply rate) is the reason why ignition does not occur in this configuration. Ignition may occur with a thicker sample under the same conditions by increasing the amount of the sample.

Ignition occurs in the angle range of approximately $+45^\circ < \theta < +80^\circ$ after a hole is formed through the sample. Why does ignition occur at these angles? And what is the role of the hole in the ignition process? The distributions of heat release rate (proportional to gas phase reaction rate) and contours of temperature and oxygen mass fraction are plotted in Fig. 15a with the formation of a hole and in Fig. 15b without the formation of a hole. The latter calculation is made with the addition of one cell layer which is inert and does not absorb the incident radiation. With formation of the hole, flow through the hole appears at $t = 0.88 \text{ s}$ in Fig. 15a and flow velocity increases up to about 5 cm/s with an increase in hole size due to consumption. The flow supplies

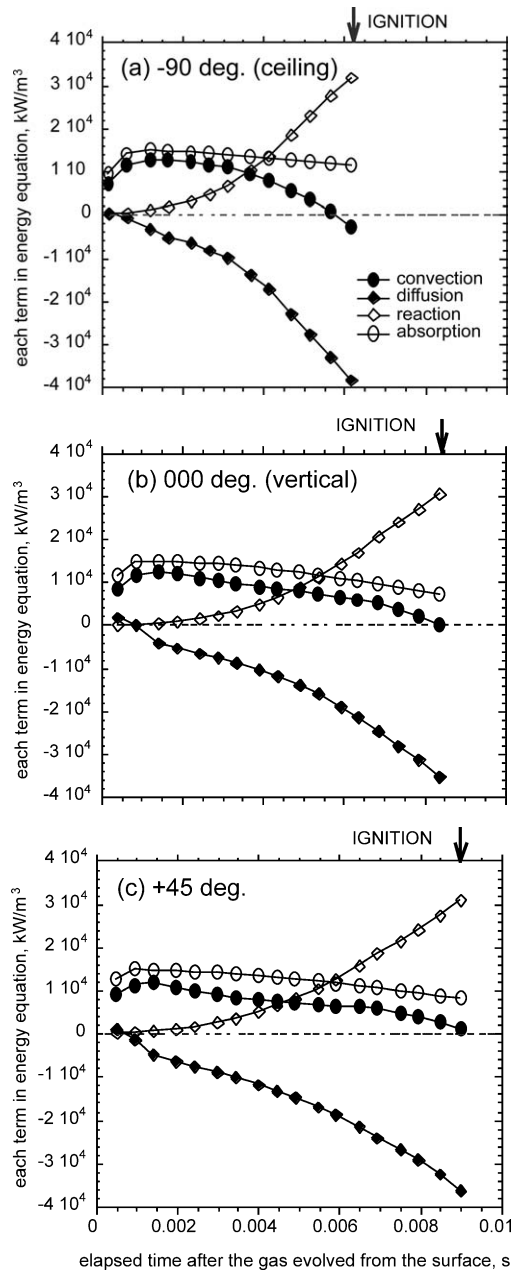


Fig. 13. Contributions of convection, diffusion, and absorption to the local temperature increase at three different angles under $Q_{\text{ex}} = 27 \text{ W}$, $\beta = 10 \text{ atm}^{-1} \text{ m}^{-1}$.

warm air (about 700 K) from the backside to the irradiated side through the hole, and the gas-phase reaction rate over the irradiated area increases gradually with an increase in the air supply rate. Without formation of the hole, on the other hand, the gas-phase reaction rate does not increase significantly, probably due to a lack of oxygen supply, as shown in Fig. 15b. Therefore, formation of the hole is critical to ignition

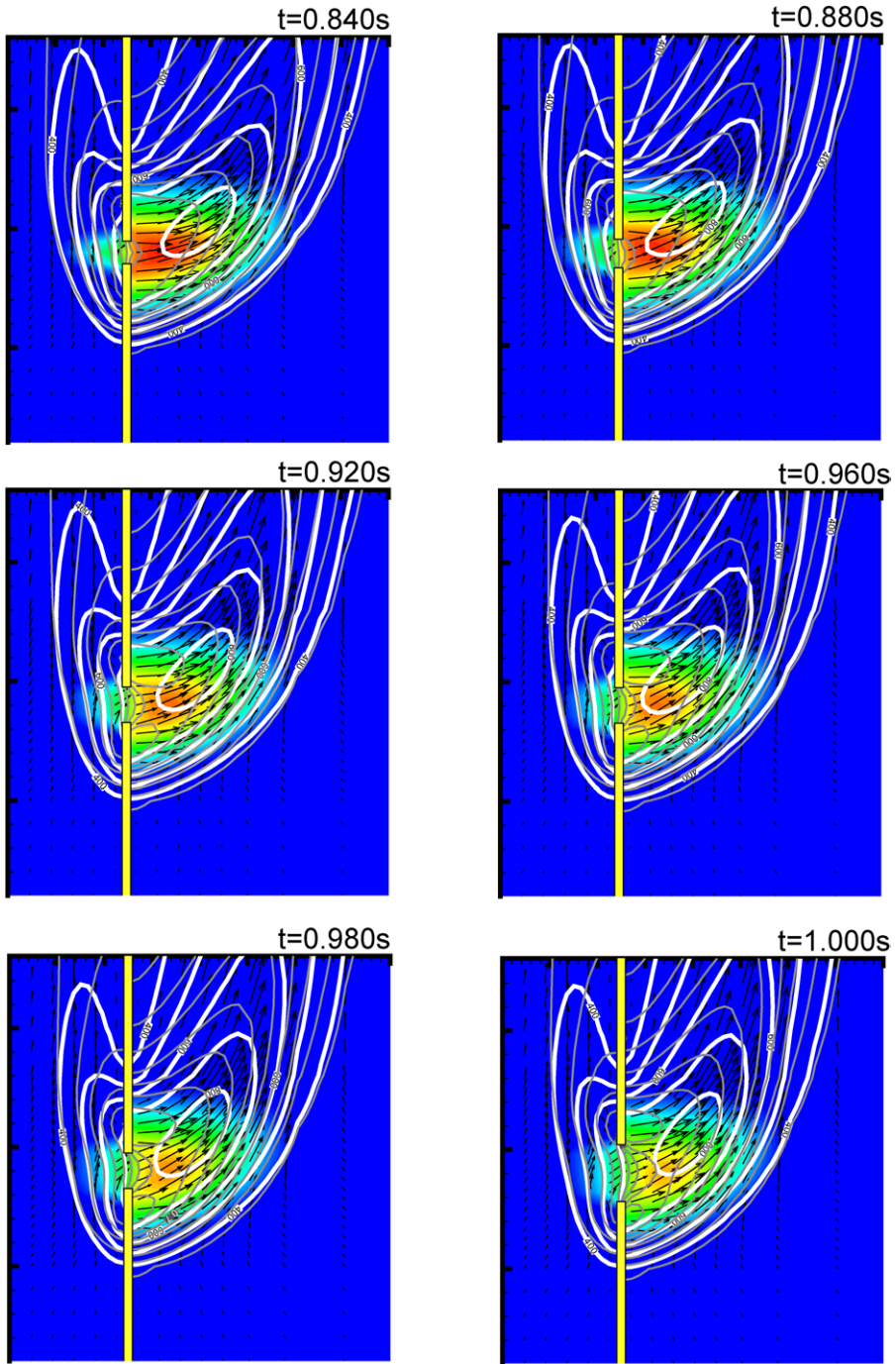
in this range of sample angle at 18.6 W of incident total radiant energy. Formation of the hole has two counteractive effects: one is total consumption of the sample, indicating that supply of fuel is declining, and the other is buoyancy-induced flow through the hole, which supplies warm air to the irradiated side. The amount of flow through the hole depends on the sample orientation angle with respect to the direction of gravity. At $\theta = 0^\circ$ (vertical orientation), the amount of flow through the hole is the lowest and this might be the reason why ignition is not achieved as shown in Fig. 14. At $\theta = +90^\circ$ (floor configuration), the amount of the flow is greatest, but incident flux irradiating the sample surface through a tall plume of MMA becomes lowest due to absorption by the MMA plume as shown in Fig. 11. This reduces the fuel supply rate and the local absorption of incident energy and so ignition does not occur in the vertical sample configuration.

An experimental study to investigate the above predicted ignition trends with respect to various sample orientation angles is in progress, and the experimental results will be compared with the numerical results for the validation of our numerical code.

5. Conclusions

Nonpiloted ignition processes of a thin PMMA sheet with a laser beam as an external radiant source were investigated using a three-dimensional, time-dependent numerical calculations to determine and understand the effects of sample orientation angle on ignition delay time in quiescent air in a normal-gravity environment and of imposed velocity in a microgravity environment. In a zero-gravity environment, ignition delay time increases with an increase in imposed flow velocity.

In a normal-gravity environment at high incident total radiant energies, ignition delay increases with an increase in sample orientation angle from -90° (ceiling configuration) to approximately that of a vertically mounted sample (the exact angle depends on incident flux and absorptivity of the evolved degradation product). Then, ignition delay time is nearly independent of the sample orientation angle. Further increase in the sample angle reduces ignition delay time, followed by a slight increase near $+90^\circ$ (floor configuration). To heat the evolved fuel gas (MMA) from the degradation temperature to around 900 K for the runaway gas-phase reaction, initially absorption of the incident radiation (laser) by MMA is most significant, followed by convective heating and, finally, exothermic heat release from the reaction near the onset of ignition. Ignition is not predicted without the laser absorption given the chemical and physical

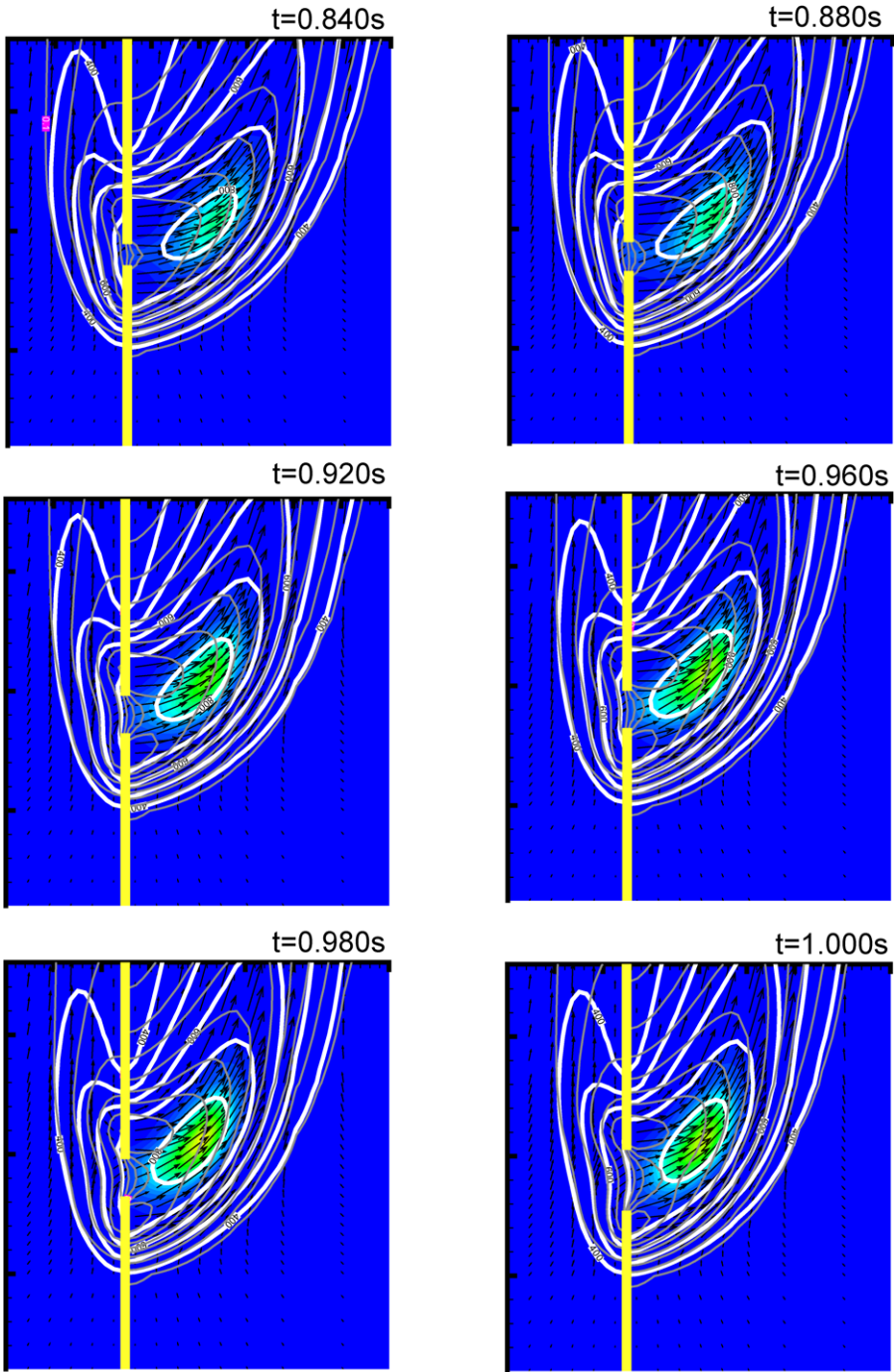


gradation: absorbed energy contour
 thick lines: temperature contour
 thin lines: MMA mass fraction contour

$Q_{ex}=18.6W$
 vertical orientation

(a)

Fig. 14. Distribution of (a) absorbed energy and (b) heat release rate with contours of temperature and MMA mass fraction at $\theta = 0^\circ$ at $Q_{ex} = 18.6 W$ with the formation of a hole through the sample.

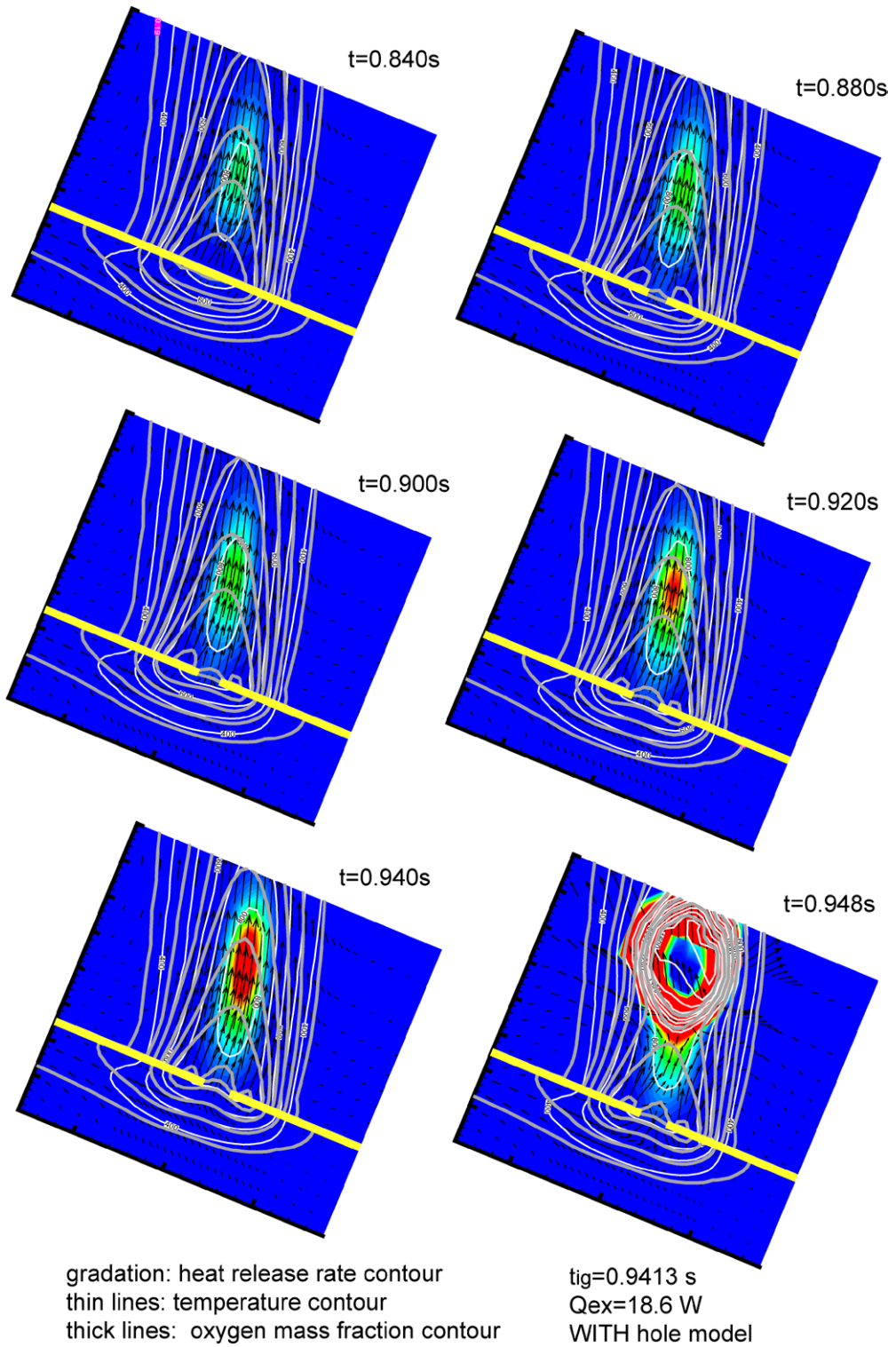


gradation: heat release rate contour
 thick lines: temperature contour
 thin lines: MMA mass fraction contour

$Q_{ex}=18.6W$
 vertical orientation

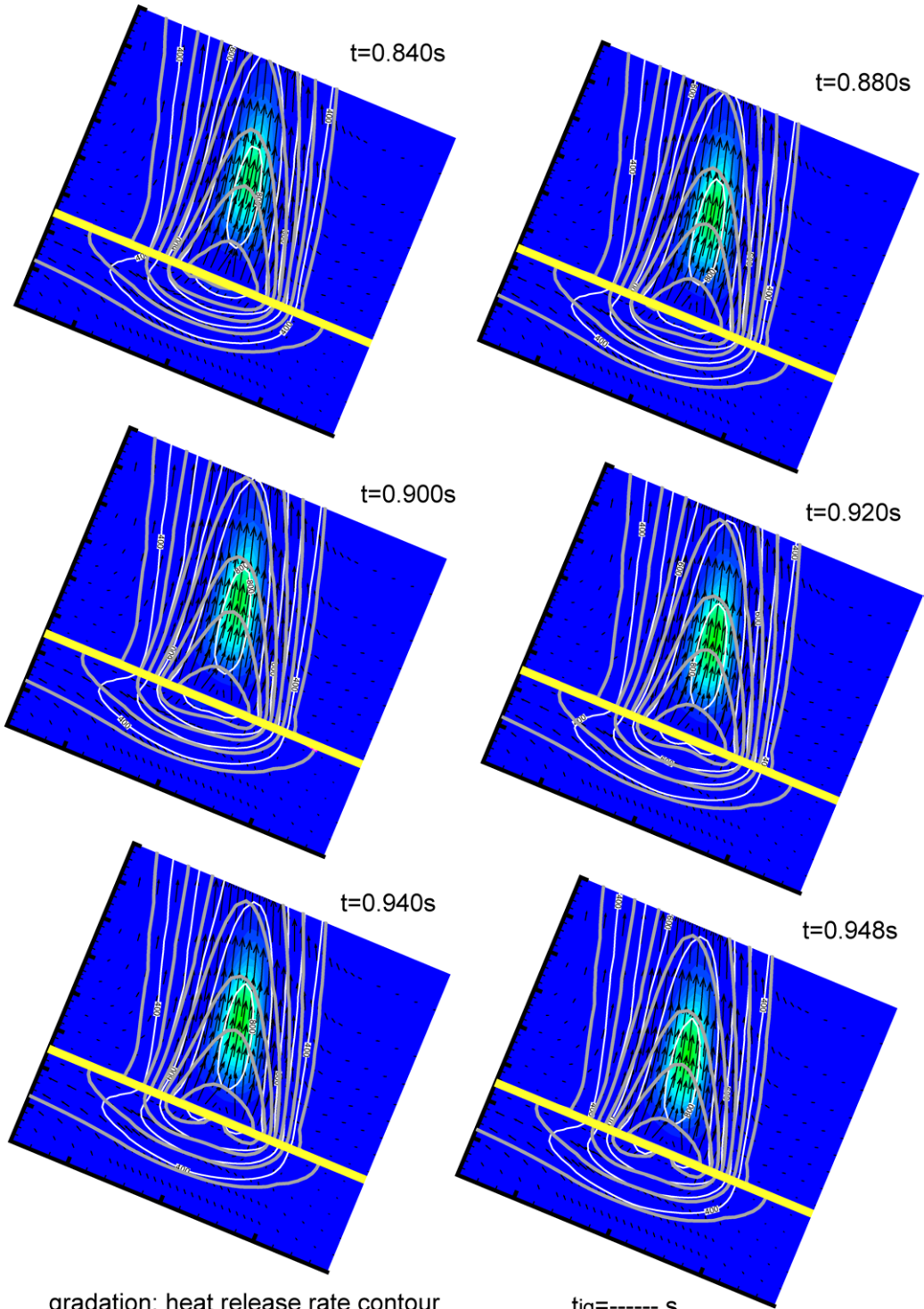
(b)

Fig. 14. Continued.



(a)

Fig. 15. Distribution of heat release rate (proportional to gas-phase reaction rate) with contours of temperature and oxygen mass fraction at $\theta = +68^\circ$ at $Q_{ex} = 18.6$ W (a) with the formation of a hole and (b) without the formation of a hole through the sample.



gradation: heat release rate contour
 thin lines: temperature contour
 thick lines: oxygen mass fraction contour

tig=----- s
 $Q_{ex}=18.6\text{ W}$
 WITHOUT hole model

(b)

Fig. 15. Continued.

properties used in this study. The gas-phase heating time is about 25% of the ignition delay time for the sample in the ceiling configuration (downward-facing sample irradiated by upward beam). With an increase in the sample mounted angle, it increases to nearly 45% for the vertically mounted sample. With a further increase in the angle, it remains above 40%. Evolution time (the time it takes the evolved degradation gas to travel from the surface to the ignition location) is 3–4% of ignition delay time for all angles. The remainder of the delay time is solid heating time.

At lower incident total radiant energies in normal gravity, ignition is not achieved in certain sample orientation angles (i.e., about $-30^\circ < \theta < +45^\circ$ at an incident total radiant energy of 18.6 W). The most favorable ignition configuration is at $\theta = 0^\circ$ (ceiling configuration). The formation of a hole through the thin sample due to total consumption has two counteractive effects on the ignition process: one is reduction in fuel supply rate, and the other is an increase in air supply from the back side to the irradiated side by the buoyancy-induced flow through the hole. The former effect appears to be dominant for the angle range of about $-30^\circ < \theta < +45^\circ$, and the latter effect becomes important in the angle range of about $+45^\circ < \theta < +80^\circ$.

Acknowledgments

This work is partially supported by the NASA Microgravity Science Program under Interagency

Agreements C-32090-K and NCC3-919, and partially funded by the Japanese Association for Disaster Prevention Research.

References

- [1] D. Drysdale, *An Introduction to Fire Dynamics*, Wiley, New York, 1985.
- [2] C. DiBlasi, *Prog. Energy Combust. Sci.* 19 (1993) 71–104.
- [3] T. Kashiwagi, *Proc. Combust. Inst.* 25 (1994) 1423–1437.
- [4] T. Kashiwagi, *Combust. Flame* 34 (1979) 231.
- [5] T. Kashiwagi, *Fire Saf. J.* 3 (1981) 185.
- [6] B. Amos, A.C. Fernandez-Pello, *Combust. Sci. Technol.* 62 (1988) 331.
- [7] S.H. Park, C.L. T'ien, *Int. J. Heat Mass Transfer.* 33 (1990) 1511.
- [8] C. Di Blasi, S. Crescitelli, G. Russo, G. Cinque, *Combust. Flame* 83 (1991) 333.
- [9] Y. Nakamura, T. Kashiwagi, K.B. McGrattan, H.R. Baum, *Combust. Flame* 130 (2002) 307–321.
- [10] K. Seshadri, F.A. Williams, *J. Polym. Sci.* 16 (1978) 1755.
- [11] L. Krishnamurthy, F.A. Williams, *Proc. Combust. Inst.* 14 (1972) 1151.
- [12] T.-H. Tsai, M.-J. Li, I.-Y. Shih, R. Jih, S.-C. Wong, *Combust. Flame* 124 (2001) 466.
- [13] T. Hirata, T. Kashiwagi, J.E. Brown, *Macromolecules* 18 (1985) 1410–1418.
- [14] J.A. Esfahani, *Combust. Sci. Technol.* 174 (2002) 183.
- [15] <http://fire.nist.gov/fds/>.
- [16] Y. Nakamura, T. Takeno, *JSME Int. J. Ser. B* 44 (2001) 288.